Volume 1 | Number 1 | Jan 2013 | Pages 1–100

Journal of
Materials Chemistry A

Materials for energy and sustainability
www.rsc.org/materialsA

Li⁺

ROYAL SOCIETY
OF CHEMISTRY

ROYAL SOCIETY
OF CHEMISTRY

www.rsc.org/materialsA

Operando X-ray Diffraction and X-ray Absorption Studies of the Structural Transformation upon Cycling Excess Li Layered Oxide Li[Li$_{1/18}$Co$_{1/6}$Ni$_{1/3}$Mn$_{4/9}$]O$_2$ in Li Ion Batteries

Ching-Hsiang Chen[1,*], Chun-Jern Pan[2], Wei-Nien Su[1], John Rick[2], Chih-Jen Wang[2], M.Venkateswarlu[2], Jyh-Fu Lee[3], Bing-Joe Hwang[2,3,*]

[1]Graduate Institute of Applied Science and Technology, National Taiwan University of Science and Technology, # 43 Keelung Road, Sec. 4, Taipei 10617, Taiwan
[2]Department of Chemical Engineering, National Taiwan University of Science and Technology, 43 Keelung Rd, Sec. 4, Taipei, 106, Taiwan.
[3]National Center for Synchrotron Radiation Research Centre, Hsinchu, Taiwan.

Operando, X-ray diffraction and X-ray absorption spectroscopic (XAS), measurements were carried out on layered Li[Li$_{1/18}$Co$_{1/6}$Ni$_{1/3}$Mn$_{4/9}$]O$_2$ to investigate the structural changes during the first charging and discharging. XRD results showed a phase transformation from rhombohedra to monoclinic during the charging process. X-ray absorption near-edge spectroscopy (XANES) measurements showed that the major charge compensation takes place at the Ni metal site as occurred through a two-step process, i.e. Ni^{2+}→Ni^{3+}→Ni^{4+}, while the cobalt ions (Co^{3+}) and manganese ions (Mn^{4+}) remain unchanged, during Li-ion insertion/de-insertion. Extended X-ray absorption fine structure (EXAFS) results at the Ni edge showed a significant distortion of the Ni-O and Mn-O shells, while no significant distortion was observed at the Co-O shell during charging and discharging. From the structural analysis results, the cobalt doped Li[Li$_{1/18}$Co$_{1/6}$Ni$_{1/3}$Mn$_{4/9}$]O$_2$ cathode was shown undergo a partially increase of oxygen ions at the Mn ions environment due to the oxygen ions migration from the bulk to the surface in the electrode's structure during charging. It indicated that the LiMn$_2$O$_3$ domain plays an important role in the oxygen-activation plateau. The mechanism also showed

that the partial amount of Co in a transition metal slab of the excess lithium layer oxide materials can stably maintain the lithium ions in the transition metal inter slabs and the surface electronic structure of oxygen ions are reversible during electrochemical cycling between 4.6V and 2.5V.

Key words: Operando, XRD, XAS, lithium batteries, layered cathode

*Corresponding author

Email: bjh@mail.ntust.edu.tw

Tel: 886-2-27376624

Fax: 886-2-27376644

Introduction

Lithium transition metal oxides have always attracted attention as candidate electrode materials for rechargeable lithium batteries. At present, $LiCoO_2$ is widely used as a cathode material in commercial lithium ion batteries, due to such advantages such as its ease of preparation, stable electrochemical cycling and its acceptable specific capacity. However, safety issues, toxicity and the poor rate performance of $LiCoO_2$ have shifted attention to other layered compounds that contain less cobalt. Among them, derivatives of Li_2MnO_3 or $Li[Li_{1/3}Mn_{2/3}]O_2$, where the transition metal layer is substituted with other transition metals (Ni, Co etc) that result in materials with a high capacity with good electrochemical behavior [1-8]. The structure of these cathode materials is an iso-structure of $LiCoO_2$ which is a well known layer structure of α-NaFeO$_2$ with a space group of $R\overline{3}m$. The Li and transition metals (Mn, Ni, Co, etc.) occupy the 3a and 3b

sites in the octahedral MO_6 symmetry [7]. The electrochemical capacities of $Li[M_xLi_{1/3}Mn_{2/3}]O_2$ (M = Ni, Co, CoNi, etc.) cathodic materials are higher than theoretically expected, i.e. they have the highest capacities among layered oxides [3, 6, 9-13]. For example, the $Li[Ni_xLi_{(1-2x)/3}Mn_{(2-x)/3}]O_2$ cathode has a theoretical capacity of 126.5 mAh g^{-1}, based on the redox potential of Ni^{2+}/Ni^{4+}; however, the experimental capacity was found to be higher than 350mAh g^{-1} [10]. The most interesting features of $Li[M_xLi_{1/3}Mn_{2/3}]O_2$ cathode materials include their super lattice structures, high specific capacities, and high working potentials. Dahn and his co-workers undertook pioneering work on $Li[M_xLi_{(1-2x)/3}Mn_{(2-x)/3}]O_2$ systems and proposed a electrochemical model to explain the anomalous charge capacity based on the active redox reactions of nickel and the removal of an electron simultaneously with the expulsion of oxygen [5,7]. Bruce and his coworkers demonstrated a large irreversible capacity was attributed to the exchange of Li^+ by H^+ and that the exchange rate is sensitive to temperature [14]. Manthiram and his group reported that a high Mn^{4+} content in solid solution $Li[Li_xM_{1-x}]O_2$ (M = Ni, Co, CoNi, etc.) causes, both the loss of oxygen and a decrease in its mobility during charging [15]. Recently, computational and nuclear magnetic resonance spectroscopy results explained the electrochemical phenomena based on charge ordering in the transition metal layer around the Mn atom [16-18]. Delmas and his coworkers reported that an irreversible structural reorganization occurs upon cycling the Li- and Mn-rich layered oxide $Li_{1.2}Mn_{0.54}Co_{0.13}Ni_{0.13}O_2$ in lithium cells. Their results showed that a mixture of two phases is formed on a high voltage plateau, which is preserved during long-range cycling [19]. Despite the considerable amount of work focused on $Li[M_XLi_{(1-2X)/3}Mn_{(2-X)/3}]O_2$ (M = Ni, Co, CoNi) systems, deeper structural characterizations are required to

understand the origin and changes in the ordering and electronic state of cations during cycling.

Among the 'next generation' cathode materials, $Li[Ni_{0.5}Mn_{0.5}]O_2$, possessing a theoretical capacity of 280 mAh g^{-1}, is a potential candidate for lithium rechargeable batteries [20-24]. However, the specific capacity is sensitive to the preparative as well as the cycle test conditions. The variation in the capacity is due to such difficulties as obtaining a relatively pure phase at a low temperature, stability, and cation mixing [20, 22, 23]. Significant improvements in the electrochemical properties with extended cycling were achieved by partial substitution of cobalt in $LiNi_xCo_{1-2x}Mn_xO_2$ [25-29]. Increasing the x value in the synthesized $LiNi_xCo_{1-2x}Mn_xO_2$ powder leads to decreased particle size and an increase in cation mixing. The electrochemical phenomena are due to the redox couple of nickel, while the substituted Co and Mn stabilizes the structure with extended cycling. In addition, the substituted cobalt can also enhance the electrical properties, thereby reducing the polarizability and minimizing the migration of Ni in the Li layer. Therefore, it is thought that the substituted cobalt in the $Li[Ni_XLi_{(1-2X)/3}Mn_{(2-X)/3}]O_2$ cathode can control the exchange of Ni and Li, enhance the rate capability, improve the thermal characteristics compared to $LiCoO_2$ and $LiNiO_2$, and stabilize the cathode's structure giving an extended cycle life. Furthermore, the increase in cobalt will suppress the super lattice structure which is believed to be responsible for the improved capacity. We have chosen an appropriate amount of cobalt in the $Li[Li_{X/3}Co_XNi_{1/2-X}Mn_{1/2-X/3}]O_2$ (x =1/6) cathode in order to get an improved electrochemical performance and at the same time maintain the super lattice structure.

It is obvious that the structural modification, and/or changes in the local environment, will occur upon lithium ion extraction and re-insertion. It is hard to confirm the phase transformation and to estimate the magnitude of lattice distortion in a multi-component electrode system by means of *ex situ* X-ray diffraction techniques. Hence, synchrotron radiation based XRD and XAS techniques have been used to determine the structural properties of materials, including the electrode materials and catalysts, and also to investigate the surface interactions of nano-sized particles, etc. [30-35].

Furthermore, operando XAS measurements will provide deep insights into the local environment around the targeted element during cycling and can also be used to investigate a variety of electrode materials for batteries [8, 16, 21, 27, 36]. Therefore, the present work is focused on the examination of changes in the local structural environment upon lithium ion extraction and re-insertion. We employed a sol-gel process to synthesize a layered cathode material ($Li[Li_{1/18}Co_{1/6}Ni_{1/3}Mn_{4/9}]O_2$) and then examined its electrochemical properties using charge-discharge measurements and its structural properties by operando, X-ray diffraction and X-ray absorption spectroscopy, techniques during charging and discharging.

Experimental Section

Electrode material preparation

$Li[Li_{1/18}Co_{1/6}Ni_{1/3}Mn_{4/9}]O_2$ was prepared by a sol–gel process using citric acid as a chelating agent. Stoichiometric amounts of various acetates such as $Li(CH_3COO).2H_2O$, $Mn(CH_3COO)_2.4H_2O$, $Co(CH_3COO)_2.4H_2O$ and $Ni(CH_3COO)_2.4H_2O$ were dissolved in 100 ml of distilled water and refluxed until completely dissolved. The solution temperature was raised to 80^0C and stirred for 4 h to form a viscous gel. The resulting gel

was dried in a vacuum oven at 120 ^{0}C for 24 h to obtain the precursor powder, which was ground and pre-calcined at 450°C for 4 h in air and re-sintered at 900 ^{0}C in an oxygen flow for 12 h. The resulting cathode powder was stored in an argon filled dry box in order to prevent damage from moisture and air.

Electrochemical measurements

Cathode film was prepared by mixing $Li[Li_{1/18}Co_{1/6}Ni_{1/3}Mn_{4/9}]O_2$ powder as an cathode active material, the conducting agents nano-sized carbon black and KS_6 graphite, and polyvinyldene difluoride (PVdF) as binder, in the weight ratio 85:3.5:1.5:10. N-methyl pyrrolidinone (NMP) was used as a solvent to prepare a slurry, which was coated on an aluminum (Al) current collector. The coated Al film was dried at 120^{0}C for 2 h and then roll pressed at 40 ^{0}C. The resulting cathode electrode film was punched to the dimensions of the 2032 type coin cell and stored in an argon filled dry box. The coin cell was assembled with $Li[Li_{1/18}Co_{1/6}Ni_{1/3}Mn_{4/9}]O_2$ as a cathode, Li metal foil as an anode, while 1M $LiPF_6$ and EC:DEC (1:1) was used as an electrolyte. The entire coin cell assembly was carried out in a dry box (MBruan, Unilab) in which the oxygen and humidity were both maintained at less than 1ppm. The electrochemical measurements were performed in the potential range of 2.5 ~ 4.6 V using a programmable battery cycle tester (Maccor model 2300) at room temperature.

Operando X-ray diffraction measurements

Operando X-ray diffraction (XRD) measurements were carried out at the high energy beam line 01C2 at the National Synchrotron Radiation Research Center (NSRRC), Hsinchu. The beam line was operated at an energy of 22 KeV. The XRD pattern was recorded using the wavelength (λ) = 1.3218Å for limited angular regions at room

temperature. The optical design for the monochromatic beam was as follows; the first mirror focusing at the beam vertically and asymmetrically cut and horizontally bendable a perfect single crystal as the diffraction object monochromatically focused the beam. A single crystal of Si (111) with about 10% asymmetric cutting was used to deliver a monochromatic beam size 1mm in diameter with a single spot at the sample, which was ~ 24 and 6 m away from the source and monochromator, respectively. A flat imaging plane was used as a 2-D area detector, able to collect diffraction patterns from the 2θ scale up to 40°. The XRD pattern was read by a MAC IPR420 off line imaging plate scanner

Operando X-ray absorption spectroscopy measurements

Operando X-ray absorption spectroscopy (XAS) measurements were performed on $Li[Li_{1/18}Co_{1/6}Ni_{1/3}Mn_{4/9}]O_2$ at room temperature. The *in situ* XAS data was collected in the transmission mode at the beam line BL17C at the National Synchrotron Radiation Research Center (NSRRC) at Hsinchu, Taiwan. The storage ring was operated with energy of 1.5 GeV and a current 300 mA. Higher order harmonics were eliminated by adjusting the Si (111) double monochromatic crystal, while energy calibration was performed at each scan using the first inflection point of the Co (7709 eV), Ni (8333 eV) and Mn (6539 eV) metal foils as a reference. The gas ionization chambers, filled with pure gasses such as Ar, He, etc., were used as detectors to collect the signals.

Soft X-ray absorption measurement

The soft X-ray absorption measurements were made at the BL20A1 station in NSCCR and its measurements were done in the total electron yield mode and fluorescence mode for O K-edge using an ultra high-vacuum (UHV) chamber with a base pressure of 1×10^{-10} Torr.

Data analysis of XANES and EXAFS

The X-ray absorption spectrum in the pre-edge region and the background of the above the edge region were fitted to straight-lines and cubic splines, respectively. The XANES spectra were obtained after subtracting the background from the overall absorption edge and then normalizing with respect to the edge jump step [37, 38]. The XANES spectra can provide information about the electronic transition and symmetry of the absorber and are sensitive to the chemical state and site symmetry. Thus the pre-edge and the edge regions of at second derivative were obtained for better evaluation of these transitions from core electrons to the unoccupied energy levels. Structural information about the changes in the local environment around the target atoms and structure parameters, such as the distance of neighboring atoms around the target atom in each coordination shell can be obtained by fitting the EXAFS data to a suitable crystallographic model. First, the background absorption arises due to changes in behavior of the out going and incoming electron wave functions, with a wave vector of k, and backscattered wave from the absorber to the next neighboring atoms. The EXAFS data was normalized $\chi(E)$ by the following equation (1):

$$\chi(k) = [\mu(E) - \mu_0(E)] / \mu_0(E) \qquad (1)$$

The normalized spectra were converted to k space and given a suitable k weighting to magnify the signal strength. The normalized data were fitted in the k-range of 3.61 to 10.2 Å for the Co edge, 3.57 to 10.1 Å for the Ni edge and 3.63 to 10.13 Å for the Mn edge. The normalized EXAFS data were Fourier transformed in r-space to separate the EXAFS contributions at different coordination shells. WinXAS (version 3.0) was employed to fit the EXAFS data and curve fitting analysis was performed in the r-space

between 0.9 to 3.1Å^{-1} for the Co edge, 0.9 to 3.02Å^{-1} for the Ni edge and 0.8 to 3.3Å^{-1} for

the Mn K-edge. The amplitude reduction factor (S_o^2) was fixed after the preliminary

refinement and scaled to the values at 0.746 for the Co edge, 0.812 for the Ni edge and

0.69 for the Mn edge: structural parameters such as inter-atomic distance (R),

coordination number (N) and the degree of disorder (or Debye -Waller) factor (σ_0^2) were

determined.

Results and Discussion

The voltage profiles for the initial charge and discharge reactions of conventional

coin-type lithium cells containing $Li[Li_{1/18}Co_{1/6}Ni_{1/3}Mn_{4/9}]O_2$ are shown in Fig.1. The

electrochemical data collected, at a slow rate of 0.2C, in the voltage range between 2.5

and 4.6V were consistent with the trends reported previously for the parent cathode,

$Li[Li_{1/3}Mn_{2/3}]O_2$, and its derivatives [5,7, 10, 14, 39]. The sample exhibits two regions

during charging and shows a clear transition between the regions. While the initial

sloping region, below about 4.6V, corresponds to the oxidation of nickel ions from Ni^{2+}

to Ni^{4+}, the trend of the plateau region around 4.6V is quite similar that of $Li[Ni_XLi_{(1-2X)/3}Mn_{(2-X)/3}]O_2$ cathodes. In our previous work, we observed oxygen-related surface

reactions during cycling on $Li[Ni_XLi_{(1-2X)/3}Mn_{(2-X)/3}]O_2$ cathodes in lithium ion batteries

by using *in situ* surfaced-enhanced Raman spectroscopy (SERS) [40]. We demonstrated

Li_2O formation during the extended plateau and found its formation on the cathode

eventually resulted in a diminished performance, leading to the production of species

related to the generation of H_2O together with LiOH. However, the plateau region

generation may be due to formation of redox pairs *i.e.* O^{2-}/O^- or the loss of oxygen from

the lattice. $Li[Li_{1/18}Co_{1/6}Ni_{1/3}Mn_{4/9}]O_2$ delivered charge and discharge capacities of 252 and 171 $mAhg^{-1}$, respectively, with a high irreversible capacity loss of 81 $mAhg^{-1}$. Thus, it is essential to investigate the structural transformations, charge-compensation mechanism and structural perturbations occurring in the sample during cycling. Operando, XRD and XAS measurements, were performed utilizing electrochemical *in situ* cells specifically designed for long term X-ray experiments.

XRD patterns of the first charge curves of $Li[Li_{1/18}Co_{1/6}Ni_{1/3}Mn_{4/9}]O_2$ and the selected points for operando measurements are shown in Fig. 2a. The cell was charged at a rate of 0.5 C in the potential range OCV - 4.6 V. As seen in Fig. 2d, the electrochemical behavior obtained from an *in situ* cell is similar to results obtained from a coin cell. However, the *in situ* cell delivered a charge capacity of 132 $mAhg^{-1}$ which is significantly lower than the charge capacity delivered by a coin cell (252 $mAhg^{-1}$), see Fig. 1. This large difference in the charge capacity might be due to an increase in the internal resistance of the *in situ* cell during charging. Figs. 2b & c show enlarged views of the XRD patterns obtained in the scattering angle range from 33.5 to 35.4^o and 62.0 to 65.0^o, respectively. As can be seen in these figures, the (003) reflection at $2\theta \approx 17.48^o$ and splitting of the diffraction peaks of (006), (012) and (018), (110) are characteristic indications of a layered structure. Peak indexing was based on the α-$NaFeO_2$ hexagonal structure. We further the calculated lattice parameters, c/a, and integrated intensity ratio. The value of $I_{(003)}/I_{(104)}$ is used to measure the degree of the cation mixing in the layered compounds. The smaller the $I_{(003)}/I_{(104)}$ value, the higher the disordering. If $I_{(003)}/I_{(104)}$ value is less than 1.2, it means that undesirable cation mixing takes place [28]. We subtracted the background as contribute from carbon and Al foil. The lattice parameters

were calculated as $\mathbf{a}$ = 2.87 Å, $\mathbf{c}$ = 14.28 Å, $I_{(003)}/I_{(104)}$ = 1.11 and c/a = 4.97. The results

indicated that the cation mixing in the layered materials is taken place. The rhombohedra

phase of $Li[Li_{1/18}Co_{1/6}Ni_{1/3}Mn_{4/9}]O_2$ gradually transformed to the monoclinic phase at the

end of charge as evidenced by the change in the diffraction peak positions to higher

scattering angles. Previously, it was observed that the monoclinic phase could be

transformed to the spinel phase during cycling for conventional layered cathode materials

[21, 22, 41]. However, in this work, a spinel like phase was not observed, this may be due

to the presence of cobalt in the structure helping to maintain structural stability during

cycling. Moreover, it can be noticed that the diffraction peak at $2\theta \approx 34.15778$ shifted to

34.9458^0 upon extraction of 0.841 Li during the charging process. This observation

suggests that the lattice parameter at the c-axis is reduced with the extraction of lithium

ions and hence, the lattice might experience some distortion, due to the

contraction/shrinkage of the electrode's structure. In order to examine these changes

microscopically   and   also   to   understand   the   local   environment   of

$Li[Li_{1/18}Co_{1/6}Ni_{1/3}Mn_{4/9}]O_2$, operando XAS measurements were performed, the results of

which are discussed below.

The   voltage   profile   of   the   *in   situ*   electrochemical   cell,   containing

$Li[Li_{1/18}Co_{1/6}Ni_{1/3}Mn_{4/9}]O_2$, during first charge and discharge cycle for experiments

performed at the Co, Ni and Mn K edges is shown in Fig. 3. It can be seen that the open

circuit potential (OCP) is comparable to that of conventional layered cathode materials.

As mentioned previously, the charge capacity obtained below 4.5 V is due to the active

redox reaction of nickel and the capacity obtained above 4.5 V is probably the

contribution from the oxygen loss. The charge and discharge capacities of 250 and 167

mAh g^{-1}, respectively, were determined during XAS measurements in the first cycle. At the end of the charge, the capacity was increased to 250 mAh g^{-1}, *i.e.* about 92% of its theoretical capacity (270 mAh g^{-1}). The charge and discharge data obtained from the *in situ* electrochemical cell for XAS measurements were similar to data obtained from a conventional coin cell. However, the potential difference between the charge and discharge curves of the *in situ* cell was slightly higher than that of the coin cell. As indicated earlier, this may be due to the high internal cell resistance of *in situ* measurements cell during charging. It has been reported that Li[Ni$_{0.2}$Li$_{0.2}$Mn$_{0.6}$]O$_2$ synthesized by a sol-gel process, delivers an initial charge capacity higher than 350mAh/g [10, 42]. However, it is believed that the substitution of a small amount of Co would reduce the initial capacity in the excess Li materials [43].

Operando XAS measurements were also used to examine the local structural environment of the Li[Li$_{1/18}$Co$_{1/6}$Ni$_{1/3}$Mn$_{4/9}$]O$_2$ cathode during cycling. The XAS spectrum generally consists of pre-edge (E < E$_0$), X-ray absorption near edge structure (XANES) (E = E$_0$ ± 10 eV), and near edge X-ray absorption fine structures (NEXAFS); in the region between 10 eV up to 50 eV above the edge and extended X-ray absorption fine structure (EXAFS), which starts approximately from 50 eV and continues up to 1000 eV above the edge. The minor features in the pre-edge region are usually due to the electron transitions from the core level to unoccupied higher energy levels (*s* → *p*, or *p* → *d*). In the XANES region, transitions of core electrons to non-bound levels with close energy occur. Because of the high probability of such transitions, a sudden raise of absorption is observed. In Near EXAFS, the ejected photoelectrons have low kinetic energy (E-E$_0$ is small) and experience strong multiple scattering by the first and even

higher coordinating shells. In the EXAFS region, the photoelectrons have high kinetic energy ($E-E_0$ is large), and single scattering by the nearest neighboring atoms normally dominates. In general, the shape of the K-edge XANES of the transition metal oxides provides unique information about the site symmetry, the nature of the bonding with surrounding ligands, while the threshold energy position of the absorption edge provides information about the oxidation state of the probed atom.

XANES spectra for selected x values at the Mn, Co, and Ni K-edges of $Li_{1-x}[Li_{1/18}Co_{1/6}Ni_{1/3}Mn_{4/9}]O_2$ during charging and discharging are shown in Figs. 4a, 5a & 6a, respectively, together with reference samples (Co^{2+} in CoO, Co^{3+} in $LiCoO_2$, Ni^{2+} in NiO, Ni^{3+} in $LiNiO_2$ and Mn^{4+} in Li_2MnO_3). Generally, pre-edge features are more distinct and better distinguishable in the second derivative. The features of second derivatives of XANES as labeled by small Greek letters (α, β, η) are also shown in Figs. 4b, 5b & 6b, respectively, for Mn, Co, Ni absorbers. The pre-edge peak of α or (α1 and α2) is distributed as an electronic excitation of the $1s$ core state to unoccupied $3d$ orbital of high spin $Mn^{4+}(t_{2g}^3 e_g^0)$, low spin $Co^{3+}(t_{2g}^6 e_g^0)$, and low spin $Ni^{2+}(t_{2g}^6 e_g^2)$ ions, respectively. In spite of the fact that the $1s$ to $3d$ transition is an electric dipole forbidden transition in an ideal octahedral symmetry, the appearance of a weak absorption peak is due to the pure electric quadrupole coupling and $3d$-$4p$ orbital mixing, originating from the non-central symmetric environment of the distortion of octahedral sites in the rhombohedral $R\overline{3}m$ space group [22]. The β peaks appear at the Mn, Co, and Ni K-edges. XANES spectra are due to the electric dipole allowed transition of a $1s$ core electron to an unoccupied $4p$ bound state with T_{1u} symmetry, which corresponds to the final states of $1s^1 c3d^4 L4p^1$, $1s^1 c3d^7 L4p^1$, and $1s^1 c3d^9 L4p^1$ for Mn^{4+}, Co^{3+}, and Ni^{2+},

respectively, with shakedown process originating from ligand-to-metal charge transfer [27, 44, 45]. Moreover, the main η peaks of the Mn, Co, and Ni K-edges XANES spectra are regarded as purely dipole-allowed $1s$ to $4p$ transitions without shakedown process, which corresponds to the final states of $1s^1c3d^34p^1$ for Mn^{4+}, $1s^1c3d^64p^1$ for Co^{3+}, and $1s^1c3d^84p^1$ for Ni^{2+}, respectively. Herein, c and L denote a $1s$ core hole and an oxygen $2p$ ligand hole, respectively. The β peak demonstrates the energy position lower than the absorption peak due to the $1s$ core electron, ascribed to the charge transfer on the more screened nucleus, showing a bound energy lower than the combined transitions relative to the unscreened excitation [46].

In Li_2MnO_3, the oxidation state of Mn exists as Mn^{4+} which implies that Mn is electrochemically inactive under normal experimental conditions. However, the derivatives of Li_2MnO_3 were found to deliver an unusually high specific charging capacity, due to oxygen loss in the electrode. When the oxygen loss is large, the tetravalent manganese reduces to maintain charge balance. To verify this in $Li_{1-x}[Li_{1/18}Co_{1/6}Ni_{1/3}Mn_{4/9}]O_2$, we have collected the operando XAS data at the Mn edge during charging and discharging as shown in Fig 4. In the pristine state, the absorption energy position of Mn edge is found to be close to the absorption energy position Li_2MnO_3 (Mn^{4+}) reference material. As the Li ion was de-intercalated, the pre-edge peak of α1 and α2 is seen to be invariant at various states in the Mn K-edge XANES spectra. This provides clear evidence that most of the Mn ions in the pristine $Li[Li_{1/18}Co_{1/6}Ni_{1/3}Mn_{4/9}]O_2$ are already in the Mn^{4+} oxidation state and are not oxidized as a result of the Li extraction. The observation shows that the absorption energies (β and η) shift slightly to high energies and that their intensities weaken gradually during the

14

charging process, indicating that lattice distortion might be induced by the Jahn-Teller active Mn^{3+} ions [47] and/or the small decrease of p character by Mn $3d$-$4p$ orbital mixing. However, the XANES shape-change of the Mn absorption edge, which is similar to that of the $LiNi_{0.5}Mn_{0.5}O_2$ [22], results largely from variations in the local structure during Li deintercalation and intercalation. For Co K-edge XANES (Fig. 5) during charging ($0 \geq x \geq 0.802$) the energy positions of β and η at different charge states (different x value) show a systematic decrease, due to the distorted CoO_6 structure associated with the small decrease of p character by Co $3d$-$4p$ orbital mixing. Also the energy positions of the pre-edge α peak and the absorption edge for Co absorber did not exhibit any significant edge shift to higher energies, suggesting that the Co oxidation state remains unchanged. Furthermore, during discharging the energy position of the Co edge with an increase in lithium ($0.802 \geq x \geq 0.267$) content was unaffected and it was close to that of the energy position of $LiCoO_2$ (Co^{3+}) reference. This result indicates that the cobalt did not participate in the electrochemical redox process during charging and discharging. In contrast, the Ni edge shifts to higher energy values during charging, this energy shift is completely reversible during discharging as shown in Fig. 6. The absorption energy position (α and β) of the nickel edge was almost coincident with that of the energy position of the NiO reference in the pristine state, indicating that the oxidation state of nickel was Ni^{2+}. However, the absorption energy position of nickel shifted towards a higher energy than that of the energy position of the $LiNiO_2$ (Ni^{3+}) reference, indicating that the nickel oxidation state increases to Ni^{4+} after charging. The possible reaction process is either a two-step reaction of Ni^{2+}/Ni^{3+} and then Ni^{3+}/Ni^{4+} or a one-step reaction of Ni^{2+}/Ni^{4+}. It should be noted that the absorption energy variation with respect

to the lithium content is not smooth and is significant at x = 0.327 during charging. This may be due to structural distortion in the lattice and it is believed that the oxidation process of nickel, involves an intermediate step of Ni^{3+}. The details will be discussed later by using quantitative energy shift values. In the reverse process, *i.e.* during discharging, the absorption energy position of nickel gradually shifted towards the lower energy region to coincide with that of the reference sample of NiO (Ni^{2+}), suggesting that the nickel is reduced to Ni^{2+} (from Ni^{4+}) and that the electrochemical process is completely reversible.

The changes in the absorption energies can be discussed more clearly based on the calculated energy shift values. The energy shifts (E-E_0) for the Ni, Co and Mn K-edges of the Li[$Li_{1/18}Co_{1/6}Ni_{1/3}Mn_{4/9}$]$O_2$ cathode were calculated using the absorption energy position (E) upon extraction and re-insertion of lithium ions during cycling by removing the absorption edge energy position (E_o) obtained from the reference sample. The absorption energy position (E_0) for the NiO is 8342.2eV, CoO is 7717.5eV and Li_2MnO_3 is 6560 eV, respectively. The calculated (E-E_0) values for various K-edges during cycling process are presented in Fig. 7. It is apparent that the energy shift value for the Co K-edge was 3.62 eV in the pristine state and increased slightly to 3.762 eV at the end of charging. The change in the energy shift is not significant compared to the energy shift of $LiCoO_2$ (Co^{3+}) (Fig. 7b), suggesting cobalt is not involved in the electrochemical process. The calculated energy shift values for both Mn and Ni absorbers are presented in Figs. 7a & c, respectively. The respective energy shifts, at the Mn K-edge, were found to be 0.03 and 0.986 eV, for pristine material and after complete charging. This change in the energy shift for Mn absorber may reveal that the distortion of the octahedral sites

increases during the first charge and decreases during discharge [48]. In the case of the Ni edge, the energy shift value was close to the NiO (0 eV at x = 0) reference. The energy shift was found to be dramatic when the lithium (x) content reaches 0.327 and the corresponding energy shift value (2.073eV) was close to the $LiNiO_2$ (Ni^{3+}) reference. The energy shift increases linearly with an increase in the x value and the corresponding energy shift value is 3.26eV when x = 0.718 at the end of the charging. It is worth mentioning that the change in the energy, with respect to x value, is an indication of actively participating nickel in the electrochemical redox process. However, the dramatic change in the energy shifts at x = 0.315 is strong evidence for the formation of a Jahn-Teller active site (Ni^{3+}), suggesting that the oxidation of Ni takes place through a two-step process ($Ni^{2+} \rightarrow Ni^{3+} \rightarrow Ni^{4+}$) rather than a one-step process ($Ni^{2+} \rightarrow Ni^{4+}$). Our results are consistent and in good agreement with the data reported for layered $LiNi_{0.5}Mn_{0.5}O_2$ and $LiNi_{1/3}Co_{1/3}Mn_{1/3}O_2$ cathode materials [22, 44, 49]. In the reverse scan, the energy shift values of Co and Mn were found to be 3.67 eV and 0.03 eV, respectively, and the energy values are comparable to their respective reference samples of $LiCoO_2$ and Li_2MnO_3 (Fig. 7a and 7b), suggesting that both Co and Mn maintain their oxidation states at 3+ and 4+, respectively, during discharging. In the case of Ni, the energy shift varies slightly when compared to Co and Mn (Fig. 7c). This variation in the energy shift before charging and after discharging in Ni K-edge, indicates that a small amount of Ni^{4+}or Ni^{3+} was not reduced to Ni^{2+}, resulting in a low discharge capacity and a large irreversible capacity during the first cycle.

The EXAFS spectra are the amplitude summation of out going and backscattering photoelectron waves. If these two waves are coherent, a constructive interference pattern

will be formed and the signal strength will be good enough to probe the changes in the

local environment. The change in local environment around the particular absorber can

be viewed through the EXAFS oscillations, while lattice distortion may be induced by

redox reaction process, involving for example Jahn-Teller (Ni^{3+}, Mn^{3+}, etc.) active ions.

In order to understand these changes clearly, structural analyses were performed.

Theoretical EXAFS parameters, such as the backscattering amplitude and the phase shift,

were calculated by FEFF 7 code to account for all possible scattering paths which were

generated from the crystallographic model of the known structure. The structural

parameters were calculated by fitting the EXAFS data to an appropriate two shell model.

The residual factor (*RF*) was calculated based on the experimental and theoretical data

using the following expression [50],

$$\frac{\sum_{i=1}^{N} / y_{\exp}(i) - y_{theo}(i) /}{\sum_{i=1}^{N} / y_{\exp}(i) /} \times 100 \qquad \text{----------- (2)}$$

Where $y_{\exp}$ is the experimental data and y_{theo} is the theoretical data points. The refinement

quality was determined with the residual factor value which was set to less than 10% for

all calculated structural parameters.

The normalized EXAFS spectra at the cobalt edge, as a function of lithium (x)

content, are presented in Figs. 8a & b during charging and discharging. As seen in these

figures, the EXAFS oscillations are uniform and small distortions are possibly due to the

change in the metal - oxygen shell and metal - metal shell induced by the structural

variation during cycling as observed from the results of operando XRD or even by Jahn-

Teller active Ni^{3+} ions. In addition, the change in the local structure may be due to the creation of vacancies which leads to disorder in the electrode's structure upon extraction of lithium ions during charging. However, we believe that local distortion would lead to the rearrangement of cations in the transition metal layer and possible charge ordering, due to the strong columbic driving force of lithium in the transition metal layer [16]. This point is discussed in detail in the text. The Fourier Transformed (FT) experimental spectra (continuous line) and fitted results (symbols) at the Co edge are shown in Fig. 9 during charging and discharging. The peaks at 1.5 and 2.5Å are due to the interactions of Co-O and Co-M (M = Ni or Mn or Li), respectively, at the first and second coordination shells (Fig. 9). The long distance peaks at 3.65 and 4.5 Å are due to the neighboring atoms to the cobalt absorber and multiple scattering effects, respectively. The intensities of Co-O and Co-M are almost uniform, with respect to the lithium content, during charging and discharging and are in good agreement with fitted data. Note that the changes are prominent above 4.5 Å with an increase of x during charging and discharging, respectively. The FT spectral features at the end of discharging are similar to those of the pristine state, suggesting that no distortion in cobalt's environment occurs during cycling.

The normalized EXAFS spectra at the Ni edge for different lithium contents during charging and discharging are presented in Figs. 10a &b. From these figures, it can be seen that the EXAFS oscillations are not uniform over the specified k-range, during both charging and discharging. The distortion clearly shows the existence of Jahn-Teller active ions (Ni^{3+}) during cycling, the magnitude can be estimated by fitting the EXAFS data. The Fourier Transformed (FT) experimental spectra (continuous line) and fitted results (symbols) for different lithium contents during cycling are shown in Fig. 11. The

first peak at 1.5 Å is ascribed to the interaction between the Ni-O, while the second peak

at 2.5 Å is attributed to the interaction between the Ni-M (M = Ni or Co or Mn) in the

second coordination shell**.** The prominent peaks at 4.5 and long distance at 5.5 Å are due

to the nearest neighboring and multiple scattering effects during cycling. The peak

intensity at the second coordination shell is slightly higher than the first coordination

shell, indicating that the near coordinated cations around the Ni ions have stronger

backscattering amplitude than that of other transition cations or the existence of Li^+ along

with other transition cations. Further, there is a significant distortion with the extraction

of lithium (x = 0.315) and re-insertion (x = 0.815), possibly due to the Jahn-Teller active

site of Ni^{3+}. This distortion causes structural modifications, due to the difference in the

ionic radii of Ni^{2+} and Ni^{3+} in the Ni^{3+}-O_6 octahedral symmetry. Interestingly, the spectral

features in the pristine material and at the end of discharging are found to be similar and

are in good agreement with the fitted data. This may be due to the rearrangement of

cations leading to structural stability after experiencing significant distortion caused by

the formation of Ni^{3+} ions during redox processes.

In order to understand the changes in the local structure around Mn, the

normalized EXAFS spectral features, as a function of its lithium content, are shown in

Figs. 12a & b at the first cycle. Note that the EXAFS oscillations at the Mn edge are quite

different from those of the Co and Ni edges and they show that the phase and amplitude

vary slightly with respect to the lithium content. As a result, the Mn was expected to

reduce to a lower oxidation state from Mn^{4+} in order to maintain the charge balance.

These changes are shown more clearly in the Fourier Transformed (FT) experimental

spectra (continuous line) and fitted results (symbols) as shown in Fig. 13 for various

lithium contents during cycling. In this figure, the first peak at 1.5 Å is due to the interaction between the Mn-O at the first shell and a peak at 2.5 Å is attributed to the Mn-M (M = Ni or Co or Mn) coordination in the second shell. A prominent peak at 4.5 Å and low intensity peak at 5.5 Å are ascribed to the neighboring atoms around the Mn absorber and multiple scattering effects, respectively. The intensity of the Mn-O and Mn-M vary with the lithium (x) content during cycling. These changes might be due to the oxygen loss in the electrode or to Jahn-Teller distortion. At the end of the discharging, the variation in the FT spectral features are similar to those of the pristine state. This result confirmed that Mn was not involved in the electrochemical process. The slight changes would lead to the possible rearrangement of cations in the MnO_6 octahedral symmetry. However, the differences in the long distance peaks at 4.5 and 5.5 Å are probably due to the pronounced multiple scattering effects. The changes in the local environment are discussed using the calculated structural parameters below.

As discussed earlier, EXAFS data analysis will provide insight information about the local environment around the absorber. If the metal gets oxidized, the local environment will change as a function of lithium content during cycling. Meanwhile, the structure may experience substantial distortion due to differences in the atomic radii of oxidized species. These changes can be better viewed using calculated structural parameters *e.g.* inter-atomic distances and the Debye-Waller factor The importance of these structural parameters at the metal-oxygen and metal-metal coordination shells of $Li[Li_{1/18}Co_{1/6}Ni_{1/3}Mn_{4/9}]O_2$ are discussed in detail. A quantitative analysis to obtain EXAFS structural parameters for Co, Ni and Mn was performed by fitting the first two peaks of the FT spectra. Curve fitting results for the Co, Ni and Mn K-edge EXAFS of

Li[$Li_{1/18}Co_{1/6}Ni_{1/3}Mn_{4/9}$]$O_2$ during charging and discharging are listed in Tables 1, 2 & 3, respectively. It is clear from these tables that the inter-atomic distance (R) value gradually decreases and increases with respect to the lithium content during cycling and implies that substantial distortion exists in the electrode's structure. In the first M-O shell, the change in the *R* values for the Co-O and Mn-O shells were found to be insignificant, during both charging and discharging. However, in case of the Ni-O shell, the change in the *R* value was found to be significant and the value changes (2.048 to 1.888 Å) with an increase of x value in Li_{1-x}[$Li_{1/18}Co_{1/6}Ni_{1/3}Mn_{4/9}$]$O_2$ from 0 to 0.718 during charging. This suggests that the valence of nickel (pristine state Ni^{2+}) is oxidized to a higher value and the cell volume changes with the x value, due to the difference in the atomic radii of nickel, *i.e.* Ni^{2+}(r = 0.69Å), Ni^{3+} (r = 0.56Å) and Ni^{4+} (r = 0.48Å). In the reverse scan, the *R* value increases untill the x value reaches 0.137, showing that the oxidation state of nickel (Ni^{4+}) is reduced to a lower value. Careful observations of the energy shift as a function of lithium content indicated that the change was observed when the x value reaches 0.327 (Fig. 7c). This clearly suggests that the redox reactions at the nickel active site are found to be two step processes, *i.e.* Ni^{2+} to Ni^{3+} and then Ni^{3+} to Ni^{4+} during charging. Similar variations were observed during the reverse scan, indicating that the reduction of Ni^{4+} to Ni^{2+} also involves a two-step processes, such as Ni^{4+} to Ni^{3+} and then Ni^{3+} to Ni^{2+}. These results are consistent with the observed XANES spectral features during cycling: suggesting that the calculated structural parameters are reasonable and that the predicated structural model was correct and the residual value was found to be ≤10%. The oxidation of Ni^{3+} to Ni^{4+} would reduce the concentration of Jahn-Teller active (Ni^{3+} ions) sites as a result substantial reduction in the structural distortion during

charging. A slight variation in the *R* value for the Co-O is attributed to the local distortion caused by formation of Ni^{3+} in the lattice during cycling. It is obvious that local disorder will occur upon the extraction of lithium ions (r = 0.74 Å) in the electrode's structure during charging. Furthermore, the magnitude of disorder in the lattice can be correlated to the "Debye-Waller factor" (σ_0^2). The calculated Debye-Waller factor for Co-O, Ni-O, and Mn-O are 2.5×10^{-3}, 4.5×10^{-3} and 3.0×10^{-3} Å^2, respectively, in the pristine state (x = 0). Note that the Debye-Waller factor increases and decreases with respect to the x value as shown in Tables 1, 2 & 3. From Table 1, it can be seen that the variation in the Debye-Waller factor with respect to the x values are relatively small at the Co-O, indicating that the coordination with oxygen is intact. A small change around the Co absorber is ascribed to the local distortion caused by Jahn-Teller active Ni^{3+} ions during cycling. In the Ni-O shell, a dramatic change in the Debye-Waller factor (5.8×10^{-3} Å^2 at x = 0.317) is observed, suggesting that a two-step redox reaction such as $Ni^{2+} \rightarrow Ni^{3+} \rightarrow Ni^{4+}$ is involved during charging. In the reverse scan, the Debye-Waller factor is found to be decreased and increases with a decrease of x. This result confirmed that the reduction of Ni^{4+} to Ni^{2+} also involves an intermediate step during discharging. These results are consistent with the XANES spectral features which confirmed the quality of the data and reliability of the structural model. In the Mn-O shell, the variation of the *R* value with respect to the *x* value has considerable interest, due to the presence of local structural distortion or variations in the electrode induced by the formation of Ni^{3+} during redox processes. As mentioned previously, the local distortion will increase the degree of disorder or Debye-Waller factor with increase of x value during cycling. The distortion in the electrode's structure is attributed to the increase of vacancy sites in the tetrahedral sites while

removing Li (r = 0.76Å) ions. The local distortion will allow the cations to be rearranged and the short range of charge ordering may be due to the shrinkage of the lattice.

In order to confirm the charge ordering, of either short range or long range order on the Co, Ni, and Mn environments, we have determined the coordination numbers (N) of Co-O, Co-M, Ni-O, Ni-M, Mn-O, and Mn-M (M = Ni or Mn or Li). In the case of oxygen coordination, it is found that the change in the N value as a function of x in $Li_{1-x}[Li_{1/18}Co_{1/6}Ni_{1/3}Mn_{4/9}]O_2$ for only the Mn-O shell is presented in Fig. 14a during charging, indicating that the generation of the oxygen loss occurs in the Mn environment. It indicates that the $LiMn_2O_3$ domain plays an important role in the oxygen-activation plateau. From this figure, it can be seen that there was no oxygen loss with the extraction of lithium ions up to x=0.439 and thereafter oxygen loss started and increased gradually during charging. Note that the calculated N value was found to be less than six for the oxygen loss ($0.439 \geq x \geq 0.813$) during charging process, implying that the cations were rearranged and the low N value and small R value, with respect to x value, suggested the formation of short range ordering rather than long range ordering around the Mn environment. In addition, we observed an interesting result that the partial coordination number of oxygen could be recovered during discharging. In order to understand the loss and gain of oxygen and its effect on the structural and electrochemical properties, we further identified the O K-edge absorption of the pristine, fully charge state at 4.6V and fully charge and discharge state at 2.5V electrodes by both total electron yield mode and fluorescence mode as shown in Fig. 15. The total electron yield mode is surface sensitive while the fluorescence yield mode is suitable for bulk study. The ligand K-edge XAS is very sensitive to the chemical environment around the ligand element and the electronic

structure of oxygen atom can be investigated intensively by Li-ion content. As we can see that the features of both peak A and peak B after charging to 4.6V and discharging to 2.5V are gone back to that of the pristine state in total electron yield mode spectra, suggesting that the hybridization between oxygen ions and cations after first electrochemical cycling would be similar to the pristine state on the surface of the layer electrode. It also implies that surface electronic structure of oxygen ions are reversible during electrochemical cycling between 4.6V and 2.5V. In the case of the fluorescence mode, it is found that the intensity ratio of between peak A and peak B after first electrochemical cycling are different than that of the pristine state, indicating that the cations around the oxygen ions are changed in the bulk of the layer electrode. Therefore the variation of the coordination number of oxygen around the Mn core ions may due to the oxygen ions migration from the bulk to the surface. Since the Debye-Waller factor and N are highly correlated, the increase and decrease of degree of disorder factor with respect to the x value indicates the local distortion induced by the Jahn-Teller active ion during redox reactions. These observations were consistent with the XANES and the electrochemical results of $Li_{1-x}[Li_{1/18}Co_{1/6}Ni_{1/3}Mn_{4/9}]O_2$. No evidence was obtained about the changes in the oxidation states of Mn^{4+} during cycling from XANES spectral features. We believe that the oxygen loss may marginally reduce the oxidation state of Mn during the first cycle and the absence of Jahn-Teller active (Mn^{3+}) ions will provide greater stability for the electrode's structure during cycling. Further, the changes in the local environment at the metal – metal coordination shell are discussed below.

Structural parameters such as R, N and $\sigma_0{}^2$ were also calculated at the metal - metal coordination shells of Co-M, Ni-M and Mn-M (M = Co, Ni and Mn) and are

compiled in Tables 1, 2 & 3. The calculated R value for the Co-M, Ni-M and Mn-M was found to be 2.85, 2.874 and 2.879 Å, respectively, at the pristine state. The change in the R values were from 2.85Å to 2.809 Å for Co-M, 2.874 to 2.828 Å for Ni-M and 2.879 to 2.837 Å for Mn-M; the respective corresponding Debye-Waller factor values were found to be 4.3 x 10^{-3} & 4.6 x10^{-3},   4.6 x10^{-4} & 4.9 x10^{-3}, 3.6 x 10^{-3} & 4.3x 10^{-3} $Å^2$ (before and after charging). These changes were attributed to the existence of Jahn-Teller active ions (Ni^{3+}) during cycling process. The decrease in R value is an indication of shrinkage of the lattice resulting in a lower N value during charging (Fig. 14). The change in the R value was attributed to the change in inter planar distance between the planes. From Tables 1-3, it can be seen that the Debye-Waller factor value was found to be higher for the Ni-M at the pristine when compared to that of Co-M and Mn-M before charging and after discharging. This result might be reasonably due to oxidation of Ni^{2+} to Ni^{4+} via Jahn-Teller active Ni^{3+} and also the large difference between atomic size of Ni^{2+} and Ni^{4+} inducing relatively higher local disorder in the electrode. An interesting comparison can be made by relating the electrochemical performance of $Li(Ni_{0.5}Mn_{0.5})O_2$, $Li[Ni_xMn_{(2-x)/3}Li_{(1-2x)/3}]O_2$ and $Li[Co_{x/2}Ni_xMn_{(2-x)/3}Li_{(1-2x)/3}]O_2$ cathode materials to their structural properties. In the case of $Li[Li_{1/18}Co_{1/6}Ni_{1/3}Mn_{4/9}]O_2$, the oxidation of nickel takes place through two steps Ni^{2+}/Ni^{3+} and then Ni^{3+}/Ni^{4+} which is similar to that of the layer $LiMn_{0.5}Ni_{0.5}O_2$ in which nickel is oxidized through a two-step process [22]. Recently, computational and experimental results showed short range charge ordering between Ni^{2+} and Mn^{4+} in the transition metal layer [17, 18, 21, 24, 51]. From our structural analysis results, only the average coordination of Mn-M is less than 6 in the pristine state. The observation suggests a possibility of short range ordering in which Mn ions are

surrounded by Li, Co, and Ni ions in an octahedral MO_6 symmetry: the backscattering

magnitude of Li is too weak to be calculated. The presence of a small amount of lithium

in the transition metal layer gives a strong columbic driving force for charge ordering

among the cations in the Mn environment. We believe that some Ni^{2+} would participate

in charge ordering unlike $Li[Ni_xMn_{(2-x)/3}Li_{(1-2x)/3}]O_2$, where the lithium 'prefers' to

coordinate with Mn rather than with Ni [17, 18]. Therefore, in this work, we believe that

Li was not extracted from the transition metal layer, due to there being no variation in the

coordination of Mn-M during cycling. This conclusion was made based on the observed

charge capacity which was lower than its theoretical capacity unlike $Li[Ni_xMn_{(2-x)/3}Li_{(1-2x)/3}]O_2$ cathode [8-10]. The calculated structural parameters were consistent with XANES

and in good agreement with electrochemical phenomena during cycling. These results

showed that the data quality was good and the low residual value indicated the structure

model was valid. From our results, it can be suggested that a similar structural analysis

can be performed for a variety of layer cathode materials to understand the relation

between electrochemical performance and structural changes in the local environment of

electrodes during cycling process.

Conclusions

A layered $Li[Li_{1/18}Co_{1/6}Ni_{1/3}Mn_{4/9}]O_2$ cathode was successfully prepared using a

sol-gel process. The phase transformation of rhombohedra to monoclinic was identified

by means of operando XRD during charging process. The oxidation states of Co, Ni and

Mn were confirmed to be 3+, 2+ and 4+, respectively, in the pristine state. The oxidation

state of both Co and Mn metals were found to be unchanged during charging and

discharging, indicating that both the transition metals are electrochemically inactive and only stabilize the structure. The structural parameters were deduced by fitting the EXAFS data and the significant variation at Ni-O and slight changes in the Debye-Waller factor confirmed that the electrochemical redox process of nickel takes place through two step process Ni^{2+}/Ni^{3+} and then to Ni^{3+}/Ni^{4+}. The Jahn-Teller active site (Ni^{3+}) induces the local structural distortion in the electrode. The results obtained from structural analysis were consistent with XANES results. The small R and low N values obtained for the Mn K-edge suggest that a short range ordering and Li preferred orientation occurred around Mn. Consequently, the electrochemical behavior of the Co stabilized excess lithium layer oxide $Li[Li_{1/18}Co_{1/6}Ni_{1/3}Mn_{4/9}]O_2$ analyzed by the operando XAS showed that the oxygen ions occurred loss in the Mn environment at the end of the charging without the extraction of Li from the transition metal layer and would migrated from the bulk to the surface during discharging.

References

1. K. Numata, C. Sakaki, S. Yamanaka, Solid State Ionics, 117 (1999) 257.

2. Z. Lu, D.D. MacNeil, J.R. Dahn, Electrochem. Solid-State Lett. 4 (2001) A191.

3. T. Ohzuhu, Y. Makimura, Chem. Lett. 2001, 744.

4. Z. Lu, J.R. Dahn, J. Electrochem. Soc. 149, (2002) A1454.

5. Z. Lu, J.R. Dahn, J. Electrochem. Soc. 149 (2002) A815.

6. K.S. Park, M.H. Cho, S. J. Jin, K. S. Nahm, Electrochem. Solid-State Lett. **7** (2004) A239.

7. Z. Lu, L.Y. Beaulieu, R.A. Donaberger, C.L Thomas, J. R. Dahn, J. Electrochem. Soc. 149 (2002) A778.

8. Y.S. Hong, Y.J. Park, K.S. Ryu, S.H. Chang, M.G. Kim, J. Mat Chem. 14 (2004) 1424.

9. Y.J. Park, X. Wu, Y.S. Hong, K.S. Ryu, S.H. Chang, Solid State Ionics 175 (2004) 305.

10. B.J. Hwang, C.J. Wang, C.H. Chen, Y.W. Tsai, M. Venkateswarlu, J. Power Sources 146 (2005) 658.

11. S. H. Kang, Y. K. Sun, K. Amine, Electrochem. Solid-State Lett. 6 (2003) A183.

12. Y.J. Park, Y.S. Hong, X. Wu, M.G. Kim, K.S. Ryu, S.H. Chang, J Electrochem. Soc. 151 (2004) A720.

13. M. Jiang, B. Key, Y. S. Meng, C. P. Grey, Chem. Mater. 21 (2009) 2733.

14. R. Armstrong, M. Holzapfel, P. Novàk, C. S. Johnson, S. H. Kang, M. M. Thackeray, P. G. Bruce, J. Am. Chem. Soc. 128 (2006) 8694.

15. T. A. Arunkumar, Y. Wu, A. Manthiram, Chem. Mater. 19 (2007) 3067.

16. W.S. Yoon, N. Kim, X.Q. Yang, J. McBreen, C.P. Grey, J. Power Sources 119-121, (2003) 644.

17. W.S. Yoon, S. Iannopollo, C.P. Grey, D. Carlier, J. Gorman, J. Reed, G. Ceder, Electrochem. Solid-State Lett. 7 (2004) A167.

18. C.P Grey, W.S Yoon, J. Reed, G. Ceder, Electrochem. Solid-State Lett. 7 (2004) A290.

19. H. Koga, L. Croguennec, M, Ménétrier, P. Mannessiez, F. Weill, C. Delmas, J. Power. Sources 236 (2013) 250.

20. Y. Koyama, I. Tanaka, H. Adachi, Y. Makimura, T. Ozhuku, J. Power Sources 119-121 (2003) 644.

21. Y.S. Meng, G. Ceder, C. P. Grey, W. S. Yoon, Y. S. Horn, Electrochem. Solid-State Lett. 7 (2004) A155.

22. W.S. Yoon, C.P. Grey, M. Balasubramanian, X.Q. Yang, J. McBreen, Chem. Mater. 15 (2004) 3161.

23. J. Reed, G. Ceder, Electrochem. Solid-State Lett. 5 (2002) A145.

24. M.S. Islam, R.A. Davies, J.D. Gale, Chem. Mater. 15 (2003) 4280.

25. S. Jouanneau, K.W. Eberman, L.J. Krause,, J.R. Dahn, J. Electrochem.Soc. 150 (2003) A1637.

26. J.K. Nagala, N.A. Chernova, M.Ma, M. Mamak, P.Y. Zavalij, M.S. Whittingham, J. Mat. Chem. 14 (2004) 214.

27. Y.W. Tsai, J.F. Lee, D.G. Liu, B.J. Hwang, J .Mat. Chem. 14 (2004) 958.

28. B.J. Hwang, Y.W. Tsai, D. Carliner, G. Ceder, Chem. Mater. 15 (2003) 3676.

29. C. H. Chen, C. J. Wang, B. J. Hwang, J. Power Sources 146 (2005) 626.

30. C. Bressler, M. Chergui, Chem. Rev. 104 (2004) 1781.

31. B.J. Hwang, Y.W. Tsai, L.S. Sarma,Y.L Tseng, D.G. Liu, J.F.Lee, J. Phys. Chem. *B* 108 (2004) 20427.

32. P. Smith, I.R. Gordon, D. Mandoli, B. Chapman, K.J. Reimer, Environ. Sci. Technol. 39 (2005) 248.

33. C. H. Chen, B. J. Hwang, J. S. Do, J. H. Weng, M.Venkateswarlu, M. Y. Cheng, R. Santhanam K., Ragavendran, J. F. Lee, J. M. Chen, D. G. Liu, Electrochem. Commun. 12 (2010) 496.

34. J. H. Cheng, C. J. Pan, C. Nithya, R. Thirunakaran, S. Gopukumar, C. H. Chen, J. F. Lee, J. M. Chen, A. Sivashanmugam, B. J. Hwang, J. Power Sources 252 (2014) 292.

35. K. F. Hsu, S. K. Hu, C. H. Chen, M. Y. Cheng, S. Y. Tsay, T. C. Chou, H. S. Hseu, J. F. Lee, B. J, Hwang, J. Power Sources192 (2009) 660.

36. B.J. Hwang, Y.W. Tsai, R.Santhanam, D.G. Liu, J. F. Lee, J Electrochem. Soc. 150 (2003) A335.

37. E.A. Stern, M. Newville, B. Ravel, Y. Yacoby, D. Haskel, Physica B, 208 & 209 (1995) 117.

38. S.I. Zabinsky, I.J. Rehr, A. Ankudinov M. Eller, Phys. Rev. B. 52 (1995) 2995.

39. D. Pasero, V. McLaren, S. de Souza, A. R. West, Chem. Mater. 17 (2005) 345.

40. S. Hy, F. Felix, J. Rick, W. N. Su, B. J. Hwang, J. Am. Chem. Soc. 136 (2014) 999.

41. B. Ammundsen, J. Paulsen, Adv. Mater. 13 (2001) 943.

42. J.H. Kim, C.W. Park, Y.K. Sun, Solid State Ionics 164 (2003) 43.

43. R. V. Chebiam, F. Prado, A. Manthiram, Chem. Mater. 13 (2001) 2951.
44. Y.W. Tsai, B.J. Hwang, G. Ceder, H.S Sheu, D.G. Liu, J.F. Lee, Chem. Mater. 17 (2005) 3191.

45. W.S. Yoon, C.P. Grey, M. Balasubramanian, X.Q. Yang, D.A. Fischer, J. McBreen, Electrochem. Solid-State Lett. 7 (2004) A53.

46. J. M. Tranquada, S. M. Heald, A. R. Moodenbaugh, Phys. Rev. B 36 (1987) 5236.

47. H. W. Chan, J. G. Duh, J. F. Lee, Electrochem. Commun. B (2006) 1731.

48. L. Simonin, J. F. Colin, V. Ranier, E. Canevet, J. F. Martin, C. Bourbon, C. Baehtz, P. Strobel, L. Daniel, S. Patoux, J. Mater. Chem. 22 (2012) 11316.

49. Y.J. Parka, M.G. Kimb, Y.S Honga, X. Wua, K.S. Ryu, S. H. Chang, Solid State Commun. 127 (2003) 509.

50. A. Aberdam, J. Synch. Radi. 5 (1998) 1287.

51. A. Van der Ven , G. Ceder, Electrochem. Comm. 6 (2004) 1045.

Figure Captions

Fig. 1   Charge – discharge curves of $Li[Li_{1/18}Co_{1/6}Ni_{1/3}Mn_{4/9}]O_2$ cathode from coin cell.

Fig. 2   XRD pattern of the $Li[Li_{1/18}Co_{1/6}Ni_{1/3}Mn_{4/9}]O_2$ cathode during charging process and inset in the enlarged view of 2theta values 32^0 to 35^0 and 62^0 to 70^0.

Fig. 3   In situ electrochemical cell charge and discharge curves of $Li[Li_{1/18}Co_{1/6}Ni_{1/3}Mn_{4/9}]O_2$ cathode.

Fig. 4   (a) Normalized XANES spectra of $Li[Li_{1/18}Co_{1/6}Ni_{1/3}Mn_{4/9}]O_2$ cathode at the Mn K-edge and (b) Second derivative of the absorption spectra during charging and discharging process.

32

Fig. 5   (a) Normalized XANES spectra of $Li[Li_{1/18}Co_{1/6}Ni_{1/3}Mn_{4/9}]O_2$ cathode at the Co
K-edge and (b) Second derivative of the absorption spectra during charging and
discharging process.

Fig. 6 (a) Normalized XANES spectra of $Li[Li_{1/18}Co_{1/6}Ni_{1/3}Mn_{4/9}]O_2$ cathode at the Ni
K-edge and (b) Second derivative of the absorption spectra during charging and
discharging process.

Fig. 7 Energy shift, $(E-E_0)$ of $Li[Li_{1/18}Co_{1/6}Ni_{1/3}Mn_{4/9}]O_2$ cathode: (a) Mn, (b) Co and (c)
Ni K-edges during charging and discharging.

Fig. 8 EXAFS oscillations of $Li[Li_{1/18}Co_{1/6}Ni_{1/3}Mn_{4/9}]O_2$ cathode at the Co K-edge: (a)
charging, (b) discharging.

Fig. 9 FT spectra of $Li[Li_{1/18}Co_{1/6}Ni_{1/3}Mn_{4/9}]O_2$ cathode at the Co K-edge during
charging, and discharging.

Fig. 10 EXAFS oscillations of $Li[Li_{1/18}Co_{1/6}Ni_{1/3}Mn_{4/9}]O_2$ cathode at the Ni K-edge: (a)
charging, (b) discharging.

Fig. 11 FT spectra of $Li[Li_{1/18}Co_{1/6}Ni_{1/3}Mn_{4/9}]O_2$ cathode at the Ni K-edge during
charging, and discharging.

Fig. 12 EXAFS oscillations of $Li[Li_{1/18}Co_{1/6}Ni_{1/3}Mn_{4/9}]O_2$ cathode at the Mn K-edge: (a)
charging, (b) discharging.

Fig. 13 FT spectra of $Li[Li_{1/18}Co_{1/6}Ni_{1/3}Mn_{4/9}]O_2$ cathode at the Mn K-edge during
charging, and discharging.

Fig. 14 Coordination number as a function of Li (x) of $Li[Li_{1/18}Co_{1/6}Ni_{1/3}Mn_{4/9}]O_2$
cathode (a) metal-oxygen and (b) metal-metal at the first and second

33

coordination shells during charging and discharging process.

Fig. 15 O K-edge spectra of (a) total electron yield mode and (b) fluorescence mode of Li[Li$_{1/18}$Co$_{1/6}$Ni$_{1/3}$Mn$_{4/9}$]O$_2$ cathode at pristine, after fully charge state at 4.6V, and after fully charge and discharge state at 2.5V.

Table 1 Structural parameters of Co K-edge of Li[Li$_{1/18}$Co$_{1/6}$Ni$_{1/3}$Mn$_{4/9}$]O$_2$ cathode.

Li$_{1-x}$(Li$_{1/18}$Co$_{1/6}$Ni$_{1/3}$Mn$_{4/9}$)O$_2$ X value	Shell	Bond length (A)	Debye Waller Factor σ^2 (Å^2)
Charging	Co-O	1.920	0.0025
0	Co-M	2.850	0.0043
0.276	Co-O	1.896	0.0028
	Co-M	2.823	0.0044
0.687	Co-O	1.877	0.0032
	Co-M	2.806	0.0047
0.802	Co-O	1.874	0.0032
Discharging	Co-M	2.809	0.0046
0.666	Co-O	1.884	0.0032
	Co-M	2.815	0.0047
0.267	Co-O	1.904	0.0027
	Co-M	2.834	0.0043

Table 2 Structural parameters of Ni K-edge of Li[Li$_{1/18}$Co$_{1/6}$Ni$_{1/3}$Mn$_{4/9}$]O$_2$ cathode.

Li$_{1-x}$(Li$_{1/18}$Co$_{1/6}$Ni$_{1/3}$Mn$_{4/9}$)O$_2$ X value	Shell	Bond length (A)	Debye Waller Factor σ^2 (Å^2)
Charging	Ni-O	2.048	0.0045
0	Ni-M	2.874	0.0046
0.327	Ni-O	1.884	0.0058
	Ni-M	2.841	0.0057
0.718	Ni-O	1.888	0.0036
Discharging	Ni-M	2.828	0.0049
0.582	Ni-O	1.895	0.0053
	Ni-M	2.832	0.0060
0.185	Ni-O	2.033	0.0073
	Ni-M	2.868	0.0053
0.137	Ni-O	2.044	0.0054
	Ni-M	2.872	0.0050

Table 3 Structural parameters of Mn K-edge of Li[Li$_{1/18}$Co$_{1/6}$Ni$_{1/3}$Mn$_{4/9}$]O$_2$ cathode.

Li$_{1-x}$(Li$_{1/18}$Co$_{1/6}$Ni$_{1/3}$Mn$_{4/9}$)O$_2$ X value	Shell	Bond length (Å)	Debye Waller Factor σ^2 (Å^2)
Charging 0	Mn-O	1.918	0.0030
	Mn-M	2.879	0.0036
0.115	Mn-O	1.919	0.0032
	Mn-M	2.866	0.0036
0.439	Mn-O	1.899	0.0039
	Mn-M	2.834	0.0042
0.603	Mn-O	1.899	0.0039
	Mn-M	2.832	0.0044
0.767	Mn-O	1.897	0.0043
	Mn-M	2.833	0.0044
0.822 Discharging	Mn-O	1.897	0.0043
	Mn-M	2.837	0.0044
0.841	Mn-O	1.899	0.0042
	Mn-M	2.834	0.0044
0.791	Mn-O	1.902	0.0041
	Mn-M	2.839	0.0044
0.506	Mn-O	1.905	0.0039
	Mn-M	2.844	0.0044
0.348	Mn-O	1.911	0.0038
	Mn-M	2.859	0.0041
0.166	Mn-O	1.924	0.0030
	Mn-M	2.882	0.0043
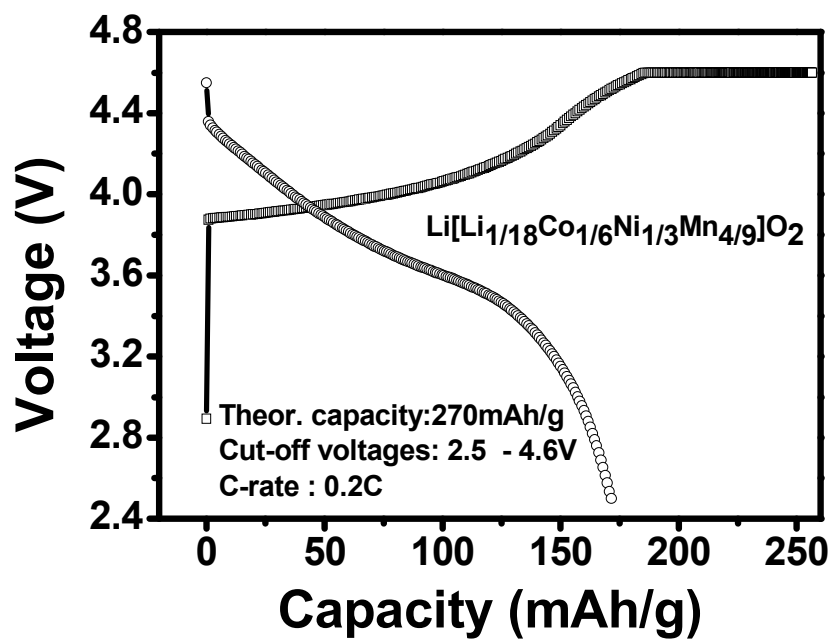
Fig. 1
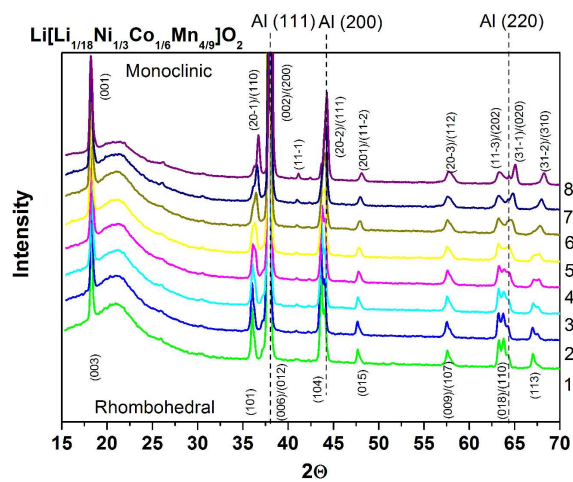
(a)
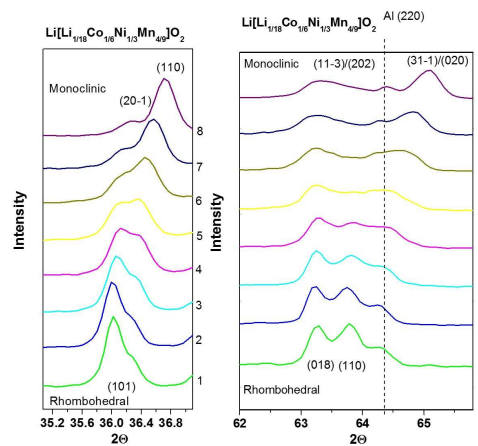
(b)   (c)
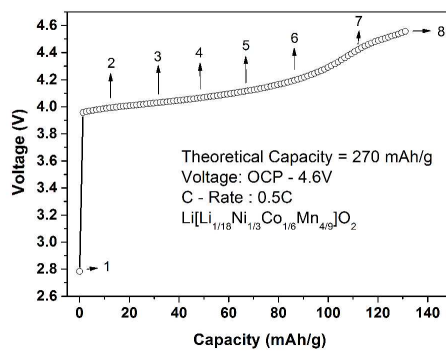
(d)

Fig. 2
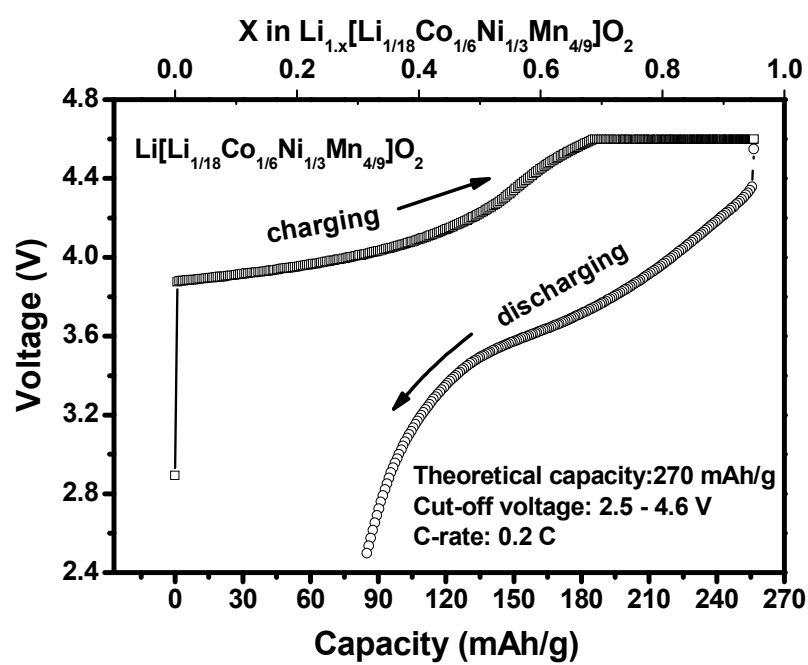
Fig. 3
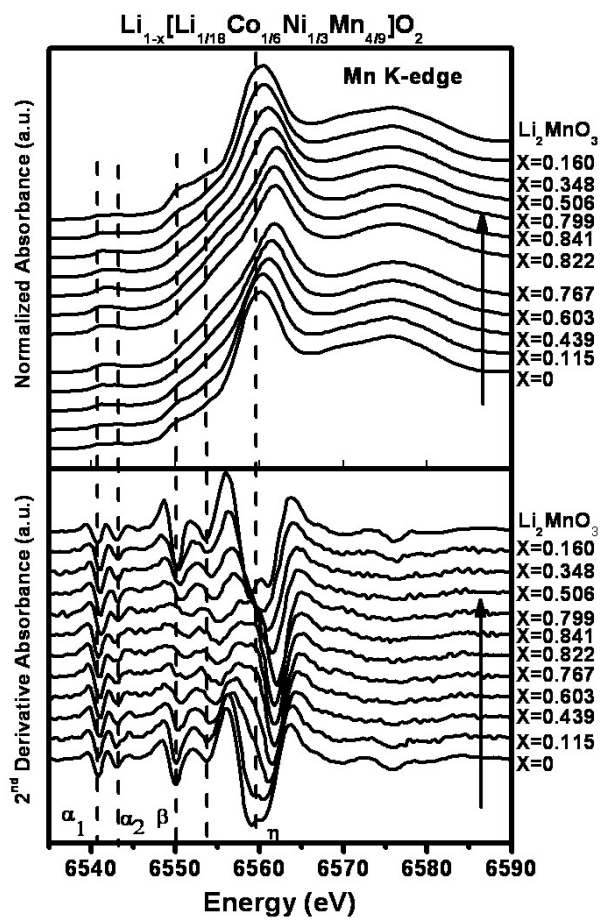
Fig. 4
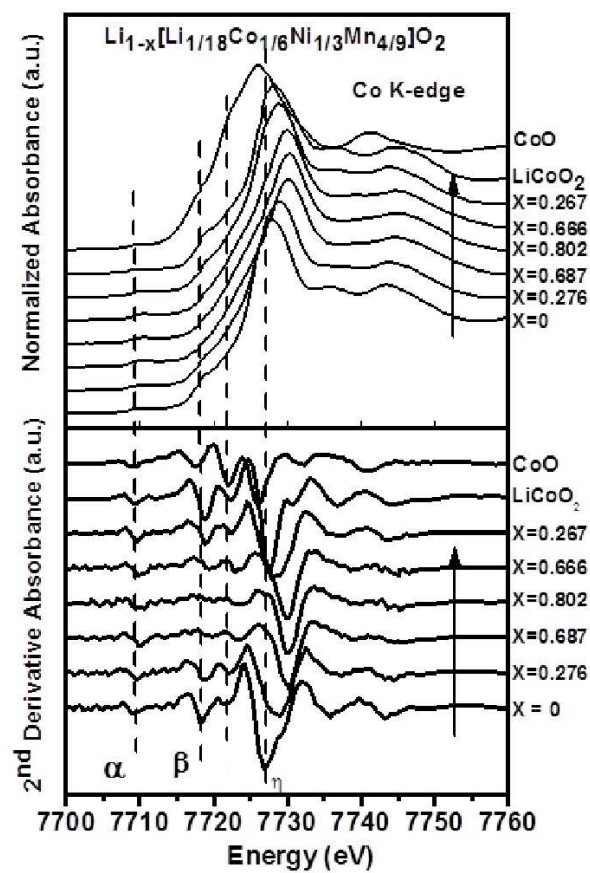
Fig. 5
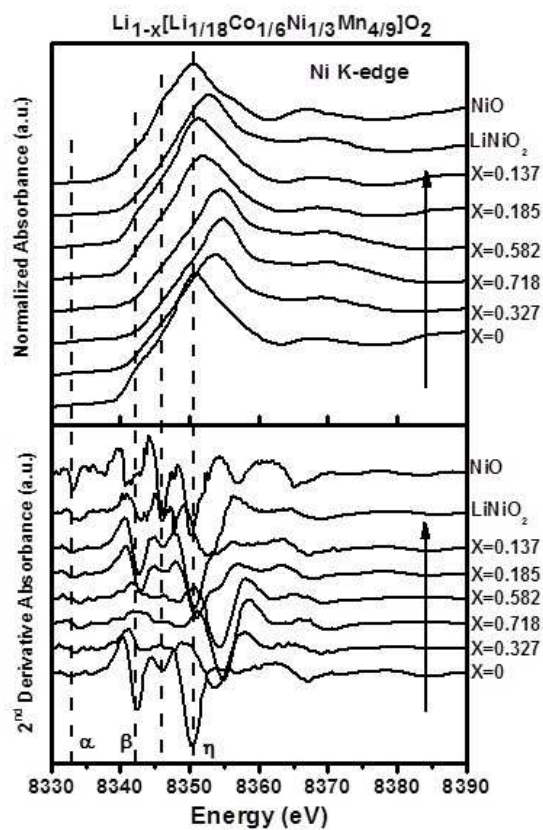
Fig. 6
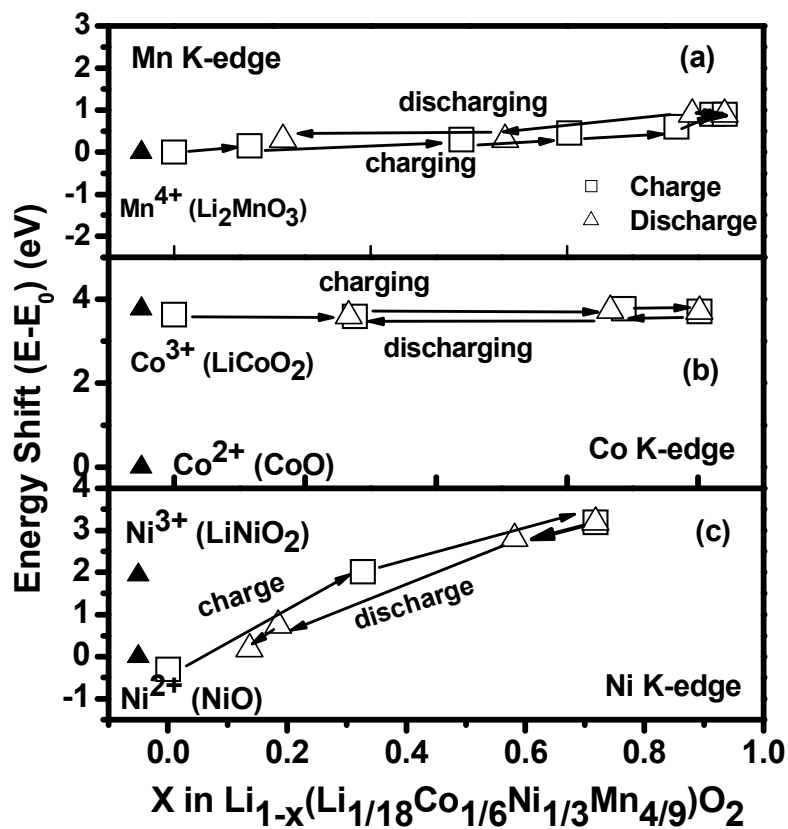
Fig. 7

(a)

(b)

Fig. 8

Fig. 9

(a)

(b)

Fig. 10.

$$Li_{1-x}[Li_{1/18}Co_{1/6}Ni_{1/3}Mn_{4/9}]O_2$$
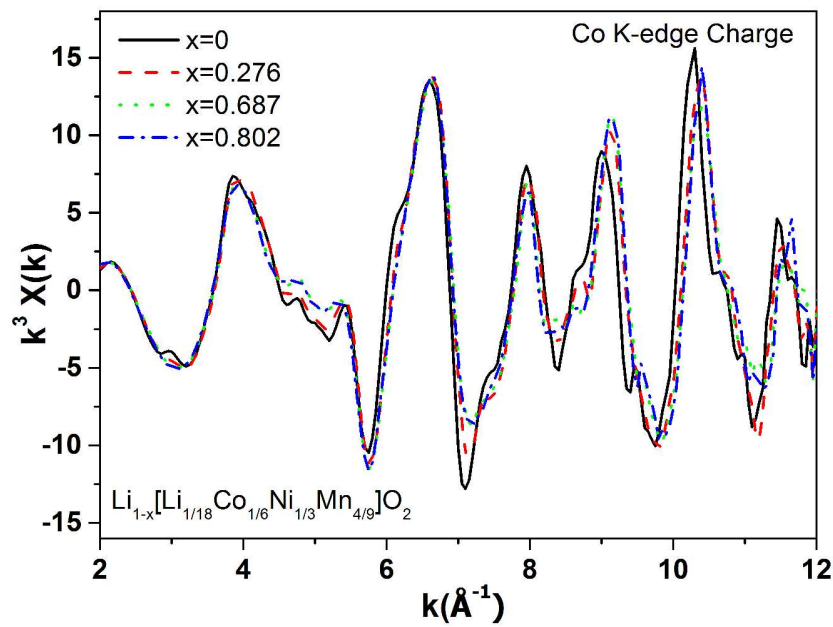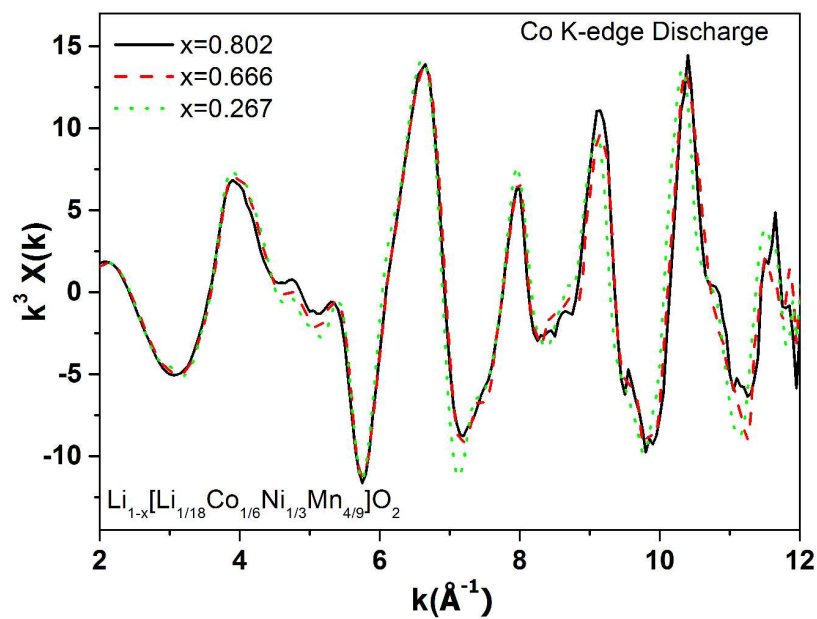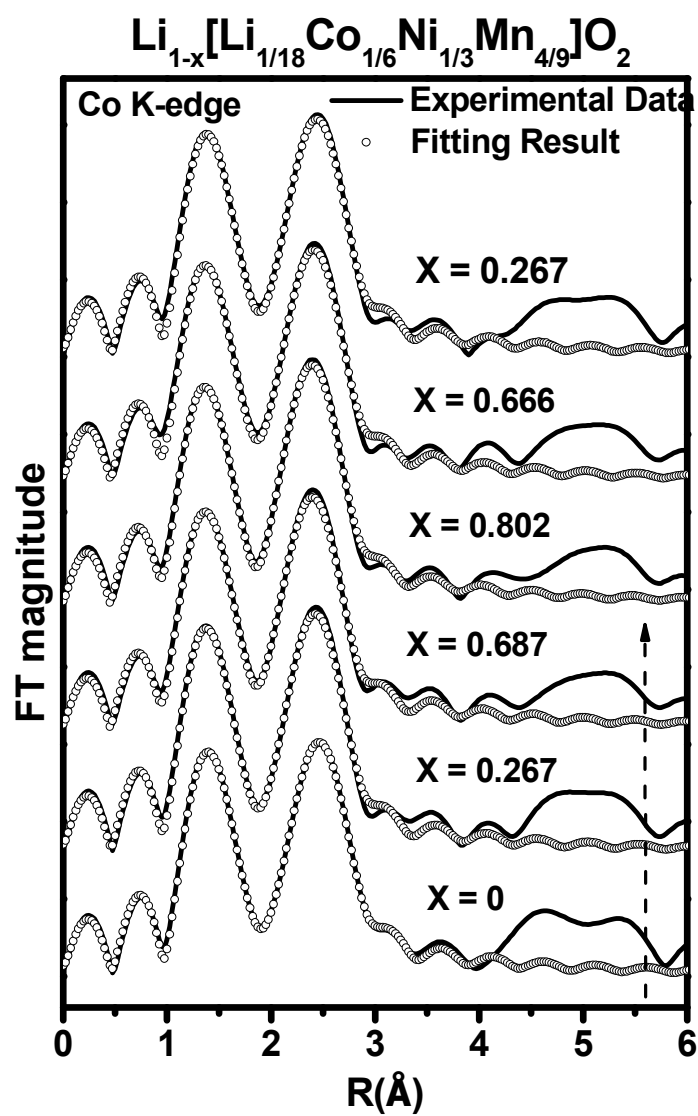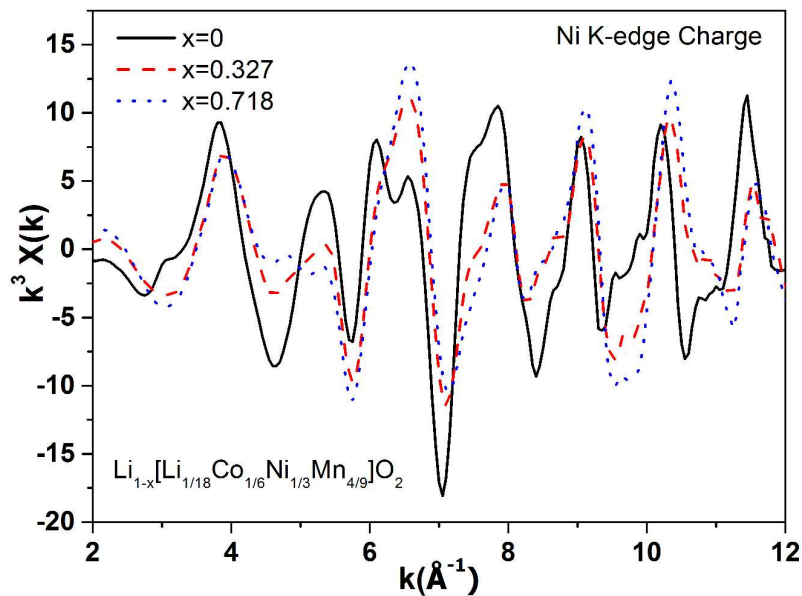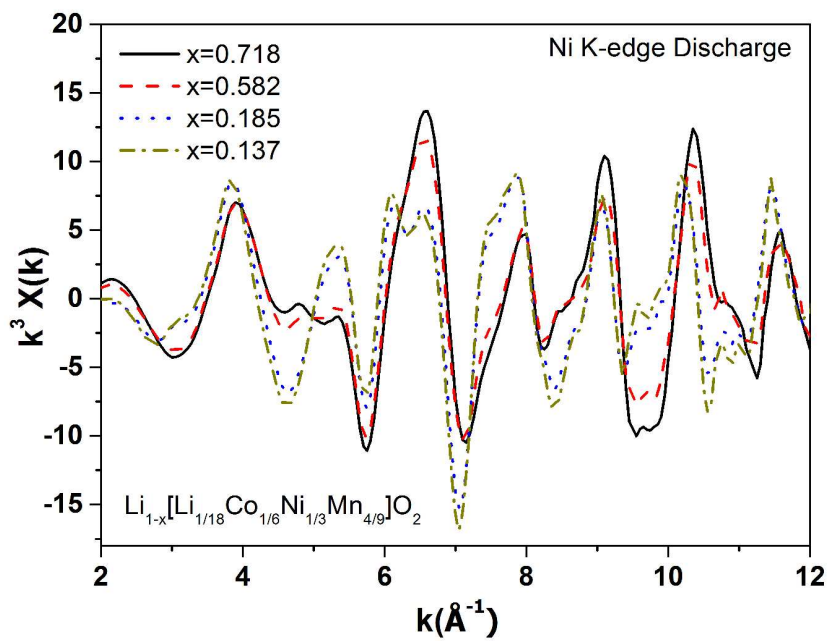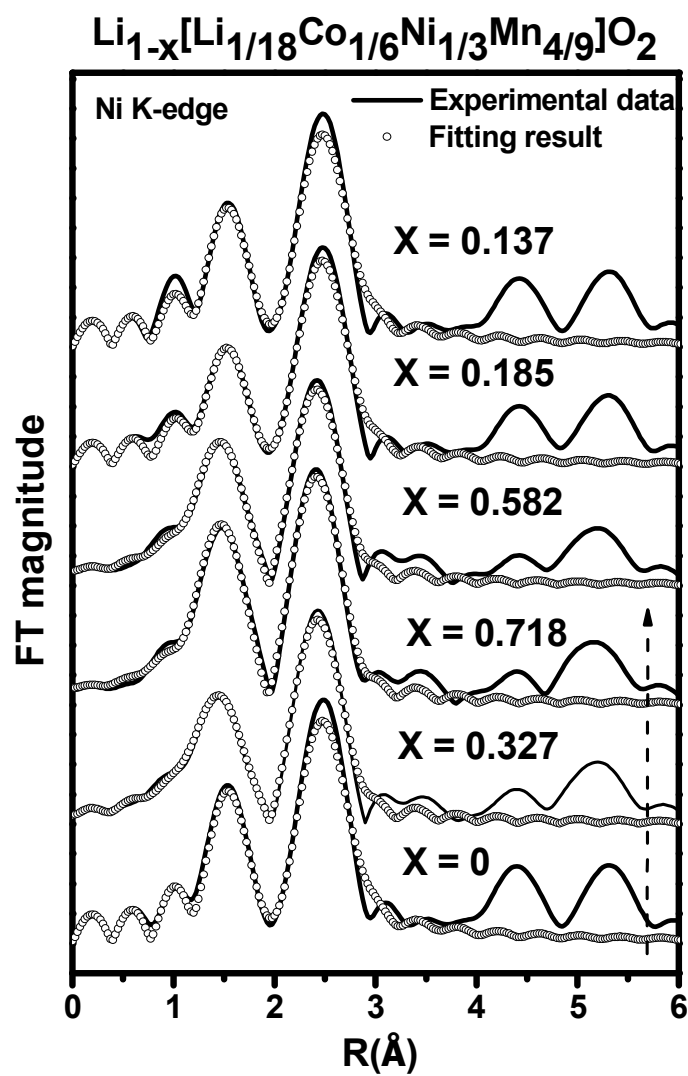
Fig. 11
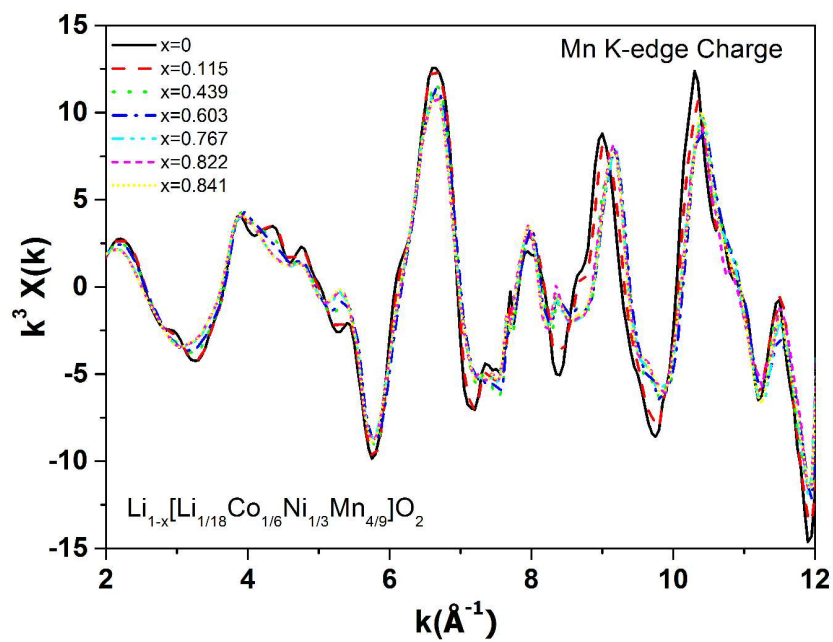
(a)
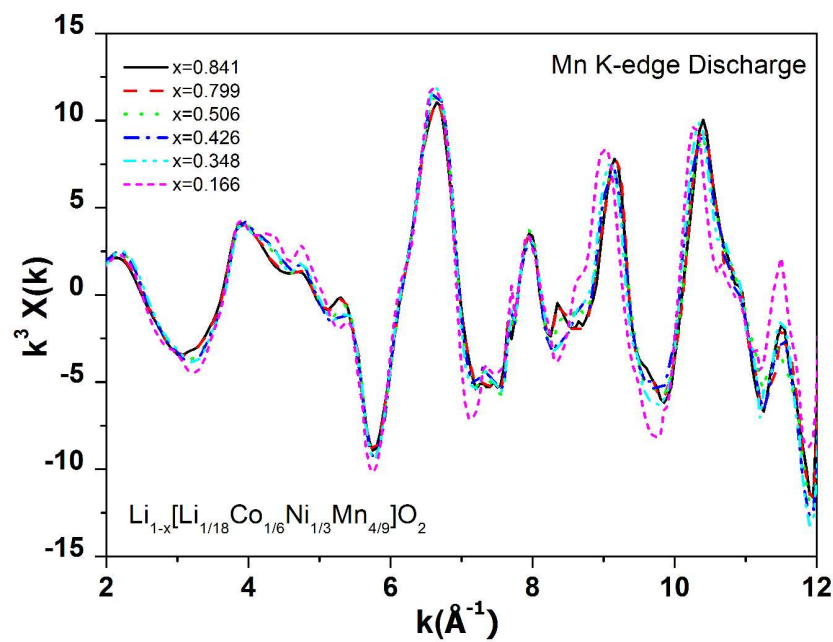
(b)

Fig. 12
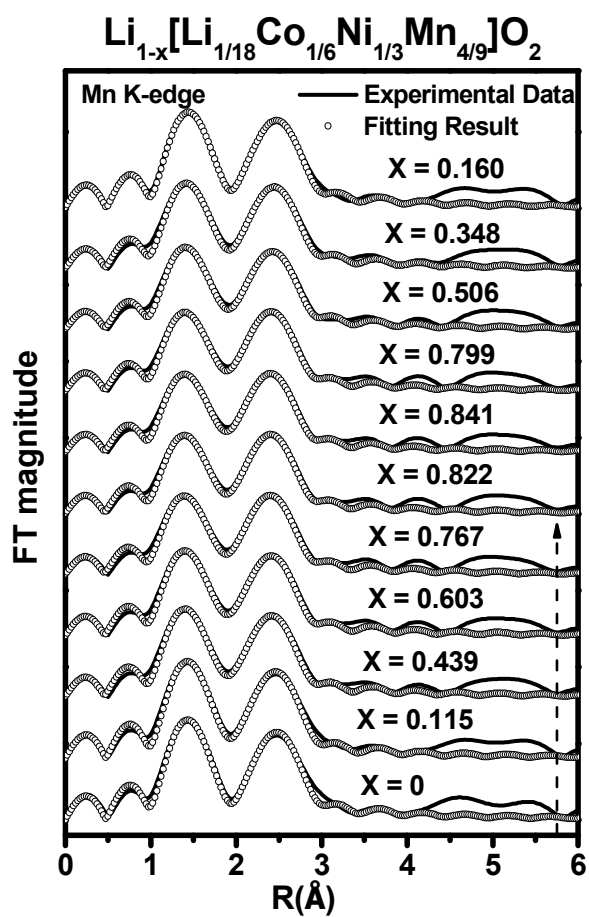
Fig. 13
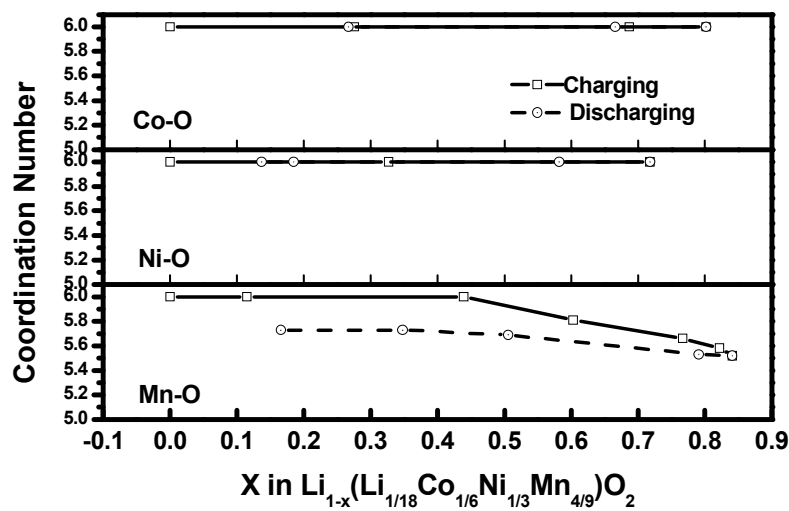
(a)
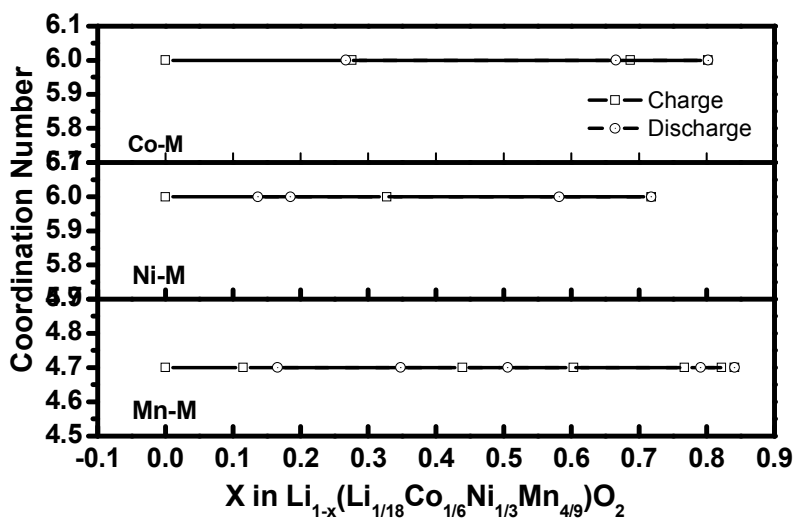
(b)

Fig. 14
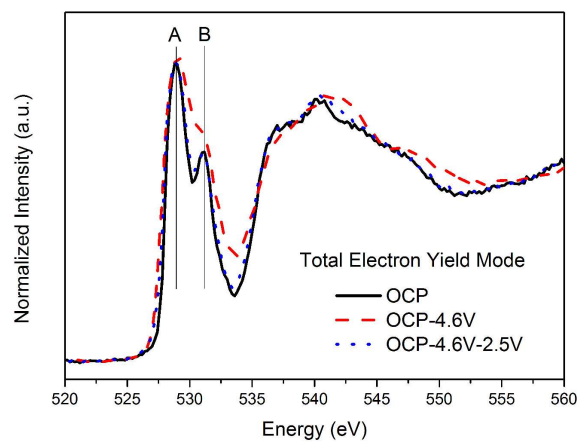
(a)
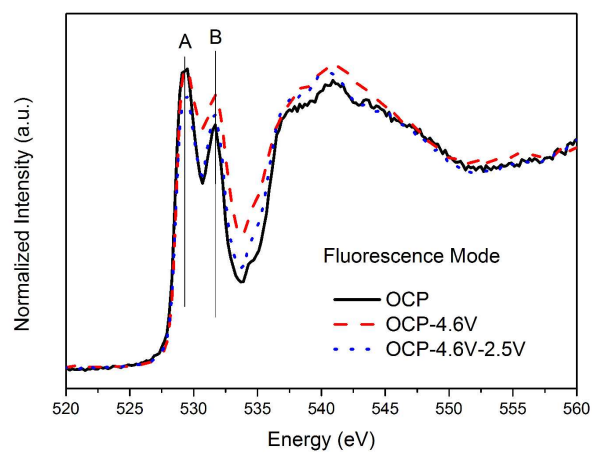
(b)

Fig. 15

TOC

The partial amount of Co in a transition metal slab of the excess lithium layer oxide materials can stably maintain the lithium ions in the transition metal inter slabs and the surface electronic structure of oxygen ions are reversible during electrochemical cycling between 4.6V and 2.5V.